第 43 卷 第 19 期/2023 年 10 月/光学学报 研究论文

光学学报

动态小凹成像光学系统

刘志强，刘豪，徐律涵，叶茂*

电子科技大学光电科学与工程学院，四川 成都 611731

摘要 如何解决大视场和高分辨率之间的矛盾成为了众多科技人员的研究重心之一。基于此，提出一种动态小凹成像系统，在传统的小凹成像系统的基础上，引入方孔液晶透镜对视场中的感兴趣区域进行扫描，实现了在除感兴趣区域外其余区域低分辨率的条件下，在特定视场内的高分辨率成像。制作了方孔液晶透镜，并且对其实际孔径的特性进行了测量与分析。搭建了基于方孔液晶透镜的成像系统，通过此系统实现了动态小凹成像，并用调制传递函数(MTF)测试卡ISO12233对感兴趣区域与其余区域的低分辨率进行了测试。

关键词 成像系统；动态小凹成像；方孔液晶透镜；高分辨率成像

中图分类号 O435.1 **文献标志码** A **DOI**：10.3788/AOS230565

1 引 言

小凹成像模拟人眼成像的特点，既可以对探测目标实现大视场的全局成像，也可以为目标细节的辨别实现局部高分辨率的成像。此技术已经被应用于场景监控、危险检测、遥感、目标跟踪等大视场成像领域来减小带宽和光学系统的复杂性。小凹成像技术最初被应用于数字视频图像处理中，作为一种数据压缩技术来加快大视频图像的传输速度和处理过程[1-3]。以前实现小凹成像的策略包括：使用非均匀传感器(具有可变感光器密度，模仿视网膜的可变采样率)[4]；设计小凹光学系统[5-7]；具有不同分辨率的独立成像器的计算集成[8-11]以及使用分割成具有不同放大倍率的多个通道的单个传感器[12-13]。但是硬件的高成本和非均匀传感器所增加的复杂性、小凹光学系统的复杂性，通常使这些解决方案没有吸引力。2001年，Martinez等[14]首次将一个空间光调制器置于一个大视场角透镜的孔径光阑处来选择性地对全视场内的期望点的像差进行校正，从而减少大视场高分辨率镜头的元件数量。然而，液晶空间光调制器对波长比较敏感，不适用于可见光波段。此外，由于其相位调制能力有限，不能矫正系统造成的离焦。Shimizu等[15]将液晶透镜放在成像系统前端用于获得图像。文献[16-19]使用液晶透镜的小凹成像系统，将透镜放在传感器和镜头模块之间，让光线在感兴趣区域内会聚，成像清晰。

本文提出一种动态小凹成像光学系统，系统由像方远心镜头、方孔液晶透镜、光学传感器、偏振片组成。像方远心镜头使像方主光线平行于光轴的特性降低了斜入射光对液晶透镜成像的影响。通过引入方孔液晶透镜对光波的相位进行调制达到局部高分辨率的目的且透镜的中心可以根据实际情况实时移动，即在保证实时检测感兴趣目标高分辨率成像的情况下，可以对整个像面进行扫描，其余区域低分辨成像。方孔液晶透镜的质量轻且体积小，整个光学系统结构更加紧凑。

2 方孔液晶透镜中心移动原理及实验结果

2.1 方孔液晶透镜结构

方孔液晶透镜[20-22]结构如图1所示，由上下两块相同玻璃基板及液晶层构成。上下基板镀有氧化铟锡(ITO)电极及高阻膜。4个电极施加正弦电压V_1、V_2、V_3、V_4。透镜的孔径为正方形边长l。

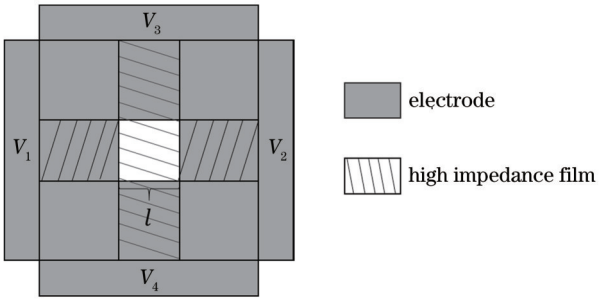

图1 方孔液晶透镜结构图

Fig. 1 Structural drawing of square hole lens

收稿日期：2023-02-17；**修回日期**：2023-03-16；**录用日期**：2023-04-17；**网络首发日期**：2023-05-08

基金项目：四川省科技计划(2021YJ0102)

通信作者：*mao_ye@uestc.edu.cn

2.2　方孔液晶透镜中心移动电场仿真

根据Kotova等[20]、Zhang等[21]的研究结果可知，当模式控制参数满足时，高阻膜区域内的电场近似线性分布。此时上下基板各处的瞬时电压 V_{upper} 和 V_{lower} 的表达式为

$$V_{\mathrm{upper}}=\frac{v_1+v_2}{2}+\frac{x(v_2-v_1)}{2},\tag{1}$$

$$V_{\mathrm{lower}}=\frac{v_3+v_4}{2}+\frac{y(v_3-v_4)}{2}。\tag{2}$$

液晶层的有效电压为 V_{rms} 的表达式为

$$V_{\mathrm{rms}}=\sqrt{\frac{\int_0^T\left(V_{\mathrm{upper}}-V_{\mathrm{lower}}\right)^2\mathrm{d}t}{T}},\tag{3}$$

式中：T 为积分时间。当上下基板的驱动电压的频率不同时，将式(1)和式(2)代入式(3)，有

$$V_{\mathrm{rms}}^2=\frac{1}{8}\left[\begin{array}{l}v_1^2(x-1)^2+v_2^2(x+1)^2+v_3^2(y-1)^2+v_4^2(y+1)^2\\-2v_1v_2(x+1)(x-1)\cos(\varphi_{21})-2v_3v_4(y+1)(y-1)\cos(\varphi_{43})\end{array}\right],\tag{4}$$

式中：$\varphi_{21}=\varphi_2-\varphi_1$；$\varphi_{43}=\varphi_4-\varphi_3$。$\varphi_1$、$\varphi_2$、$\varphi_3$、$\varphi_4$ 和 v_1、v_2、v_3、v_4 分别为正弦电压的相位和振幅且方程为椭圆方程。

由此可以得到，有效电压的中心点的坐标为

$$x_0=\frac{v_1^2-v_2^2}{v_1^2+v_2^2-2v_1v_2\cos(\varphi_{21})},\tag{5}$$

$$y_0=\frac{v_3^2-v_4^2}{v_3^2+v_4^2-2v_3v_4\cos(\varphi_{43})}。\tag{6}$$

从式(5)和式(6)可以看出，中心点的坐标由 φ_1、φ_2、φ_3、φ_4 和 v_1、v_2、v_3、v_4 共同决定。仿真结果如图2所示，驱动参数如表1所示，由图2(a)～(d)可以看出，中心移动前后电场的梯度和大小保持不变。图4中所用向列相液晶的寻常光折射率为1.513，非寻常光折射率为1.774，液晶盒盒厚为30 μm，使用波长为532 nm的激光观察液晶盒随电压的亮暗变化，得到了液晶相位延迟随有效电压的变化曲线。考虑到图4液晶材料对电压的响应，图2中电场等势线较密的区域表示液晶透镜的实际孔径。

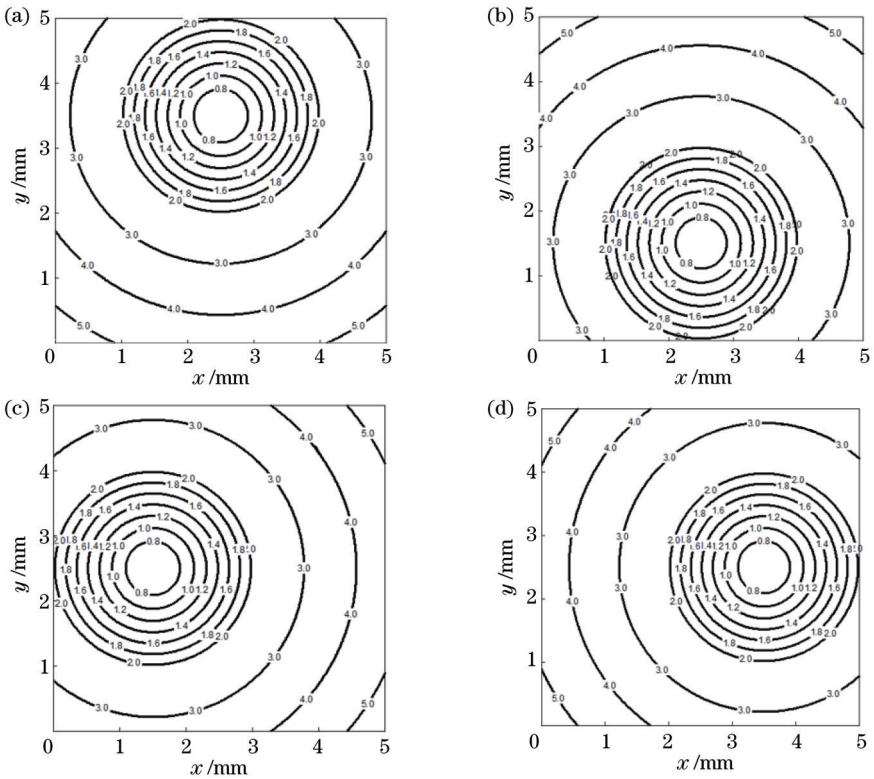

图2　电场仿真结果图。(a)中心坐标为(0,1)；(b)中心坐标为(0,−1)；(c)中心坐标为(−1,0)；(d)中心坐标为(1,0)

Fig. 2　Electric field simulation result diagrams. (a) The center coordinate is (0, 1); (b) the center coordinate is (0, −1); (c) the center coordinate is (−1, 0); (d) the center coordinate is (1, 0)

2.3　方孔液晶透镜测量结果与分析

选用与图4相同的液晶材料(江苏合成有限公司，HTW137700-100)，按照图1中的结构制作了通光孔径为5 mm × 5 mm的正方形液晶透镜，透镜的高阻膜

表 1　不同电场中心移动位置参数表

Table 1　Parameter table of moving position of different electric field centers

Icon number		Fig. 2 (a)	Fig. 2 (b)	Fig. 2 (c)	Fig. 2 (d)
Central coordinate (x_0, y_0)		(0,1)	(0,−1)	(−1,0)	(1,0)
Amplitude	v_1/V_{rms}	3.25	3.25	4.53	1.97
	v_2/V_{rms}	3.25	3.25	1.97	4.53
	v_3/V_{rms}	4.53	1.97	3.25	3.25
	v_4/V_{rms}	1.97	4.53	3.25	3.25
Phase	$\varphi_1=\varphi_3$	0°	0°	0°	0°
	φ_2/(°)	165	162.3	162.3	165
	φ_4/(°)	162.3	165	165	162.3

材料为氧化锌掺铝且阻值为 3×10^6 Ω/□，液晶盒盒厚为 30 μm。利用马赫-曾德尔干涉测量了在表 1 驱动条件下液晶透镜的干涉条纹，具体如图 3 所示。可以看出，液晶透镜实际孔径小于通光孔径，并且液晶透镜的驱动电压不同时透镜位置不同。同时由图 4 可以看出：当有效电压大于 0.6 V 小于 1.52 V 在液晶的线性响应区间内时，相位延迟与有效电压呈近似线性关系；当电压大于 1.52 V 时，响应曲线处于非线性区；当电压大于 2 V 时，液晶趋于饱和状态。所以根据式(5)、(6)和图 2 的电场仿真结果取图 3 液晶透镜中心点为原点，圆形区域以内为液晶透镜的实际孔径且直径为 1.56 mm。对图 3 的液晶透镜的有效区域进行分析可知，透镜中心不同时的光焦度为 $8.2D$，像差为 $(0.1\pm0.02)\lambda$，同时得到了透镜实际孔径。液晶透镜中心不同时的波前图如图 5 所示，可以看出透镜的波前保持不变。

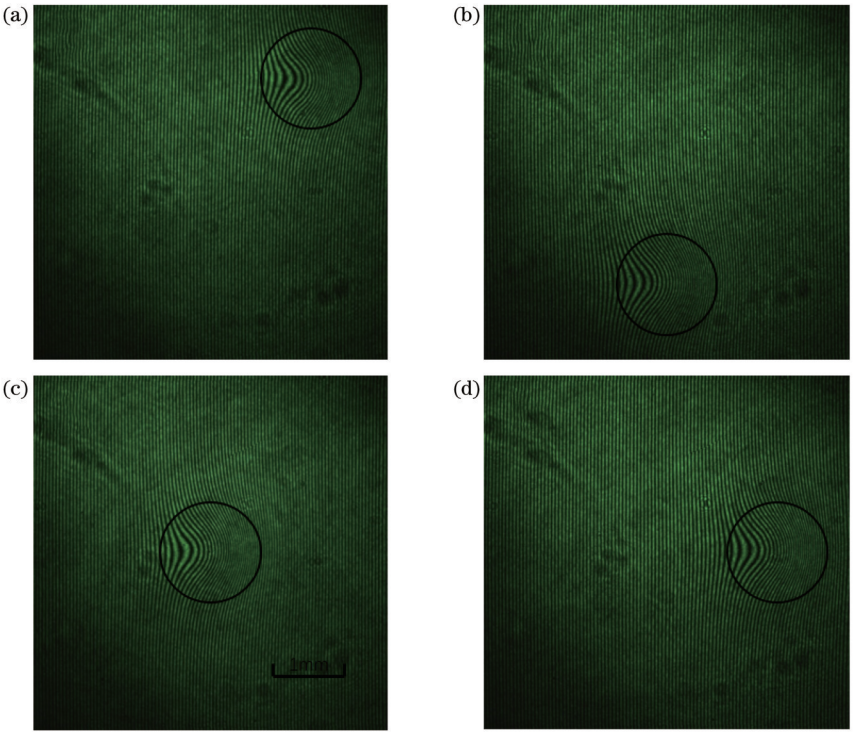

图 3　液晶透镜的干涉条纹。(a)～(d)液晶透镜中心坐标分别为(0,1)、(0,−1)、(−1,0)、(1,0)

Fig. 3　Interference fringe of liquid crystal lens. (a)-(d) The center coordinates of the liquid crystal lenses are (0,1), (0,−1), (−1,0), (1,0)

3　动态小凹成像实验及结果

动态小凹成像系统由偏振片、像方远心透镜组、方孔液晶透镜和互补金属氧化物半导体器件(CMOS)组成，图 6 为实验装置示意图，图 7 为实验装置实物图。从图 6 可以看出，一束平行光束入射到偏振片，偏振片的偏振方向与液晶透镜的摩擦方向平行，偏振光束经像方远心镜头到达方孔液晶透镜，由图 3 可知方孔液晶透镜的实际孔径小于通孔孔径，所以到达 COMS 的光部分被调制，即光束一部分聚集成像。换句话说，方孔液晶透镜置于像方远心透镜组与 CMOS 之间用于调焦并且对感兴趣区域(IA)进行实时监控，调焦及对感兴趣区域实时监控的过程由电场驱动，无需任何机械装置。图 6 中方孔液晶透镜浅色部分为通光区域，浅蓝色部分为某时刻实际液晶透镜的位置，像方远心镜头组使像方主光线平行于光轴，减少斜入射光对液晶透镜成像的影响。以图 7 方孔液晶透镜通光区域的中心为直角坐标系的原点建立如图 8 所示的直角坐标系，其中，虚线方框内为通光区域，即扫描区域，液晶透镜的中心可以在通光区域的任意位置移动且透镜的实

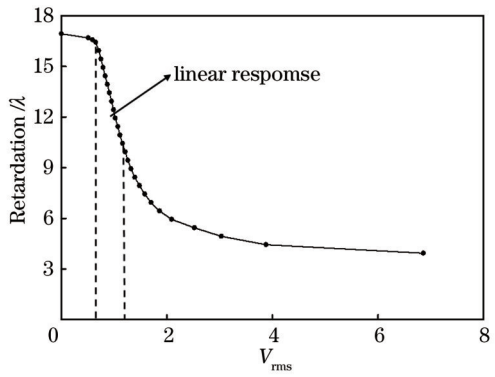

图 4　液晶随电压的响应曲线

Fig. 4　Response curve of liquid crystal with voltage

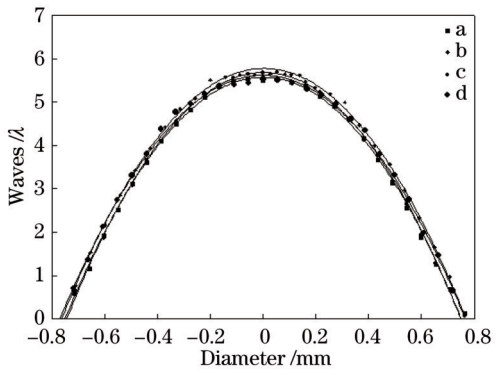

图 5　液晶透镜中心不同时的波前图

Fig. 5　Wavefront diagram of liquid crystal lens with different centers

际孔径的大小可以通过改变驱动电压来改变。选取表 1 的驱动条件来驱动液晶透镜，即中心坐标为(0，−1)、(0，1)、(1，0)、(−1，0)，实际液晶透镜的孔径直径为 1.56 mm。图 8 所示的圆形区域为不同时刻液晶透镜实际位置，实验结果如图 9 所示。可以看出，所提光学系统实现了动态小凹成像，并且利用调制传递函数(MTF)测试卡 ISO12233 对图 9 感兴趣区域与其余区域的低分辨率进行了测试，结果如图 10 所示。由图 10 可以看出，小凹部分的分辨率高于其余区域的分辨率。所用像方远心透镜组为日本 Kenko Tokina 生产的 KCM-1841MP5，焦距为 18 mm，F 数范围为 1.4～16。CMOS 的大小为 1/2 inch(1 inch=2.54 cm)，像素尺寸及截止频率分别为 2.2 μm 和 227 lp/mm。整个光学系统的视场角(水平×垂直)为 20.4°×15.4°。光路中的物距为 49 mm，像距为 20 mm，像方远心透镜组到方孔液晶透镜的距离为 12 mm，方孔液晶透镜到 COMS 的距离为 8 mm，像方远心透镜组的光圈为 8。由于液晶材料的限制，本系统的工作光波段为 400～1200 nm。

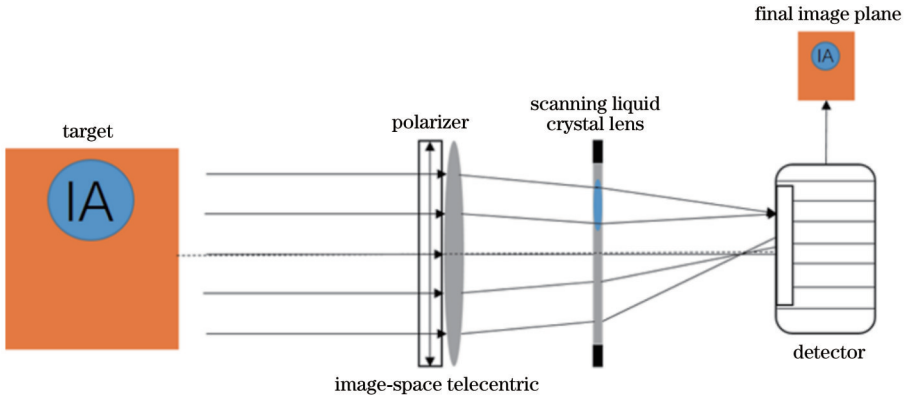

图 6　动态小凹成像实验装置示意图

Fig. 6　Schematic diagram of the dynamic foveated imaging experimental device

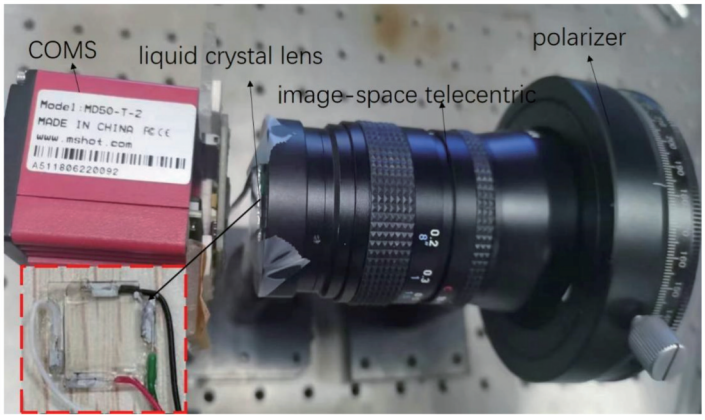

图 7　动态小凹成像实验装置图

Fig. 7　Dynamic imaging foveated experimental device diagram

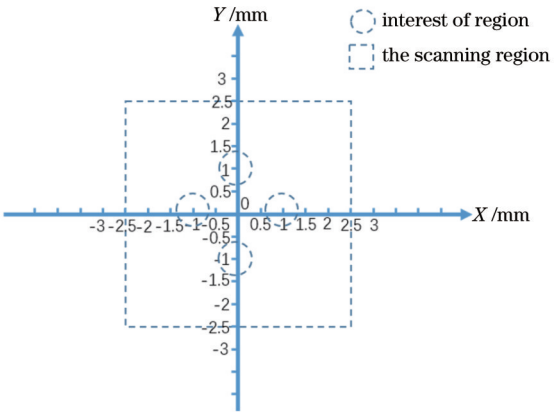

图 8　液晶透镜扫描及感兴趣区域示意图

Fig. 8　Schematic diagram of liquid crystal lens scanning and area of interest

4　结　　论

通过引入方孔液晶透镜改变光程差来实现动态小凹成像，模拟仿真了液晶透镜中心移动时的电场分布，并通过马赫-曾德尔干涉仪测量了对应电场分布下液晶透镜的干涉条纹。实验结果表明，所提动态小凹成像系统实现了感兴趣区域高分辨率成像，其余部分低分辨率成像的功能。相比于传统的光学系统，所提动态小凹成像系统不仅具有结构紧凑、光学材料简单、零级衍射效率高、传输带宽小等小凹成像系统的优势，同时也可对不同视场进行扫描并进行高分辨率成像。因此，该动态小凹成像光学系统可以应用于扫描识别、跟踪定位等领域中。

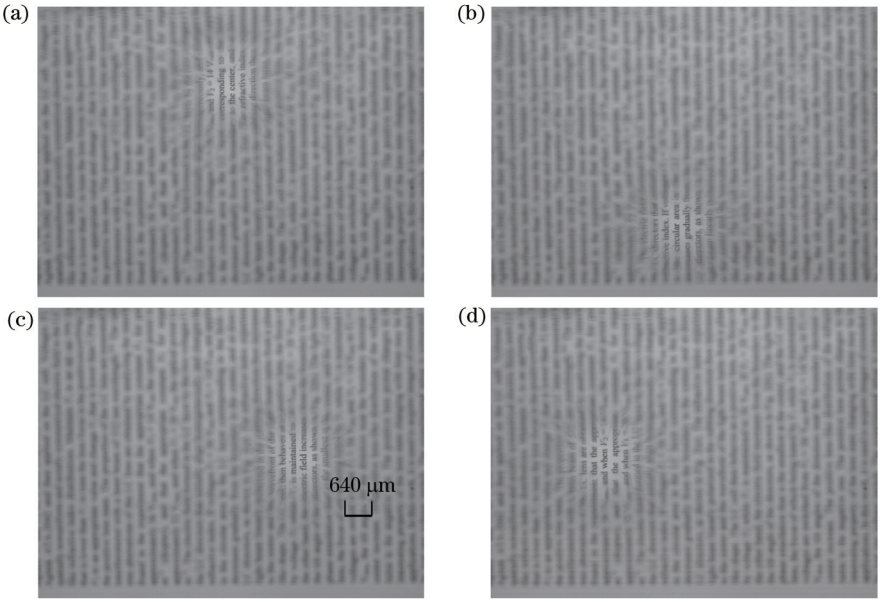

图 9　动态小凹成像实验结果图。(a)～(d)液晶透镜中心坐标(0,1)、(0,－1)、(－1,0)、(1,0)对应的小凹图像

Fig. 9　Results of the dynamic foveated imaging experiment. (a)-(d) The small foveated images corresponding to the center coordinates of the liquid crystal lens (0,1), (0,－1), (－1,0), and (1,0)

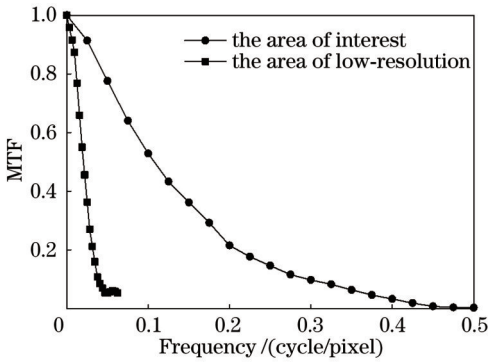

图 10　动态小凹成像系统的感兴趣区域与其余低分辨率区域的 MTF 曲线

Fig. 10　MTF curves of the region of interest and the low-resolution region of the dynamic foveated imaging system

参　考　文　献

[1] Geisler W S, Perry J S. Real-time foveated multiresolution system for low-bandwidth video communication[J]. Proceedings of SPIE, 1998, 3299: 294-305.

[2] Chang E C, Mallat S, Yap C. Wavelet foveation[J]. Applied and Computational Harmonic Analysis, 2000, 9(3): 312-335.

[3] Narayanan R M, Kane T J, Rice T F, et al. Considerations and framework for foveated imaging systems[J]. Photonics, 2018, 5(3): 18.

[4] Sandini G, Questa P, Scheffer D, et al. A retina-like CMOS sensor and its applications[C]//Proceedings of the 2000 IEEE Sensor Array and Multichannel Signal Processing Workshop. SAM 2000 (Cat. No. 00EX410), March 17, 2000, Cambridge, MA, USA. New York: IEEE Press, 2000: 514-519.

[5] Suematu Y, Yamada H. A wide angle vision sensor with fovea-design of distortion lens and the simulated images[C]//Proceedings of IECON '93 - 19th Annual Conference of IEEE Industrial Electronics, November 15-19, 1993, Maui, HI, USA. New York: IEEE Press, 2002: 1770-1773.

[6] Kuniyoshi Y, Kita N, Sugimoto K, et al. A foveated wide angle lens for active vision[C]//Proceedings of 1995 IEEE International Conference on Robotics and Automation, May 21-27, 1995, Nagoya, Japan. New York: IEEE Press, 2002: 2982-2988.
[7] Dallaire X, Thibault S. Wide-angle lens miniaturization through foveated imaging[J]. Proceedings of SPIE, 2015, 9626: 96261A.
[8] Hua H, Liu S. Dual-sensor foveated imaging system[J]. Applied Optics, 2008, 47(3): 317-327.
[9] Thiele S, Arzenbacher K, Gissibl T, et al. 3D-printed eagle eye: compound microlens system for foveated imaging[J]. Science Advances, 2017, 3(2): 1602655.
[10] Ude A, Gaskett C, Cheng G. Foveated vision systems with two cameras per eye[C]//Proceedings 2006 IEEE International Conference on Robotics and Automation, 2006. ICRA, May 15-19, 2006, Orlando, FL, USA. New York: IEEE Press, 2006: 3457-3462.
[11] Qin Y, Hua H, Nguyen M. Multiresolution foveated laparoscope with high resolvability[J]. Optics Letters, 2013, 38(13): 2191-2193.
[12] Carles G, Chen S Q, Bustin N, et al. Multi-aperture foveated imaging[J]. Optics Letters, 2016, 41(8): 1869-1872.
[13] Belay G Y, Ottevaere H, Meuret Y, et al. Demonstration of a multichannel, multiresolution imaging system[J]. Applied Optics, 2013, 52(24): 6081-6089.
[14] Martinez T, Wick D V, Restaino S R. Foveated, wide field-of-view imaging system using a liquid crystal spatial light modulator [J]. Optics Express, 2001, 8(10): 555-560.
[15] Shimizu S, Sato S. Towards non-mechanical wide angle fovea sensor: fundamental design by liquid crystal lens cell[C]//IECON 2015 - 41st Annual Conference of the IEEE Industrial Electronics Society, November 9-12, 2015, Yokohama, Japan. New York: IEEE Press, 2016: 3632-3637.
[16] Wang S C, Chen X X, Yang Y J, et al. Foveated imaging using a liquid crystal lens[J]. Optik, 2019, 193: 163041.
[17] 万超杰, 刘志强, 徐律涵, 等. 利用光轴可移动液晶透镜的立体图像采集系统[J]. 光学学报, 2023, 43(3): 0311002.
Wan C J, Liu Z Q, Xu L H, et al. Stereo image acquisition system using optical axis movable liquid crystal lens[J]. Acta Optica Sinica, 2023, 43(3): 0311002.
[18] 冯文斌, 刘志强, 徐律涵, 等. 一种高性能液晶透镜的设计方法[J]. 光学学报, 2023, 43(2): 0223001.
Feng W B, Liu Z Q, Xu L H, et al. Design method for high-performance liquid crystal lens[J]. Acta Optica Sinica, 2023, 43(2): 0223001.
[19] 胡轶瑶, 刘志强, 孙涛, 等. 利用液晶透镜实现的局部变倍成像系统[J]. 光学学报, 2022, 42(23): 2311001.
Hu Y Y, Liu Z Q, Sun T, et al. Local zoom imaging system using liquid crystal lens[J]. Acta Optica Sinica, 2022, 42(23): 2311001.
[20] Kotova S P, Patlan′ V V, Samagin S A. Tunable liquid-crystal focusing device. 1. Theory[J]. Quantum Electronics, 2011, 41(1): 58-64.
[21] Zhang Y L, Li G Y, Chen X X, et al. Driving methods for liquid crystal lens with rectangular aperture and four voltages[J]. Japanese Journal of Applied Physics, 2021, 60(10): 102002.
[22] Xu L H, Zhang Y L, Liu Z Q, et al. Liquid crystal lens with four driving voltages and its applications in imaging system with rectangular aperture[J]. Japanese Journal of Applied Physics, 2021, 61(2): 028001.

A Dynamic Foveated Optical Imaging System

Liu Zhiqiang, Liu Hao, Xu Lühan, Ye Mao*
School of Optoelectronic Science and Engineering, University of Electronic Science and Technology of China, Chengdu 611731, *Sichuan, China*

Abstract

Objective The foveated imaging simulates the characteristics of human eye imaging, which can achieve global imaging of detection targets with a large field of view and realize local high-resolution imaging for target detail discrimination. This technology has been applied to the large field of view imaging such as scene monitoring, danger detection, remote sensing, and target tracking, so as to reduce the complexity of bandwidth and optical systems. The strategies for implementing foveated imaging in the past include non-uniform sensors with variable photosensitive density for imitating the variable sampling rate of the retina, designs of foveated optical systems, calculation integration of independent imagers with different resolutions, and a single sensor with multiple channels segmented into different magnification ratios. However, the high cost of hardware, the complexity added by non-uniform sensors, and the complexity of foveated optical systems, usually make these solutions unattractive. We propose a dynamic foveated optical imaging system consisting of an object-side telecentric lens, a liquid crystal lens with a rectangular aperture, an optical sensor, and a polarizing film. The object-side telecentric lens reduces the effect of oblique incident light on the imaging of the liquid crystal lens by making the main image ray in the object plane parallel to the optical axis. By introducing a liquid crystal lens with a rectangular aperture to modulate the phase of light waves, the system achieves local high-resolution imaging, and the center of the lens can be moved in real time according to actual situations. In other words, while ensuring high-resolution imaging of the target of interest in real-time detection, the entire image plane can be scanned, and other areas have low-resolution imaging. The lightweight and small volume of the liquid crystal lens with a rectangular aperture makes the entire optical system more compact.

Methods The same liquid crystal material (HTW137700-100, Jiangsu Hecheng Co. Ltd.) in Fig. 4 is used to fabricate a liquid crystal lens with a rectangular aperture, with a clear aperture of 5 mm×5 mm according to the structure in Fig. 1. The high impedance film material of the lens is aluminum-doped zinc oxide with a resistance of 3×10^6 Ω/□, and the thickness of the liquid crystal cell is 30 μm. The interference fringes of the liquid crystal lens under the driving conditions in Table 1 are measured by using Mach-Zehnder interferometry (Fig. 3). It can be seen that the actual aperture of the liquid crystal lens is smaller than the clear aperture, and the position of the lens varies with the driving voltage. The ordinary refractive index of the nematic liquid crystal used in Fig. 4 is 1.513, and the extraordinary refractive index is 1.774. With a laser of wavelength 532 nm, the bright/dark changes of the liquid crystal cell with voltage are observed, and the phase delay of the liquid crystal is obtained as a function of the effective voltage. It can be seen that within the linear response range of the liquid crystal, which is between 0.6 V and 1.52 V, the phase delay is approximately linearly related to the effective voltage. When the voltage is higher than 1.52 V, the response curve is in the nonlinear region, and when the voltage is higher than 2 V, the liquid crystal tends to be saturated. Therefore, according to Eqs. (5) and (6) and the electric field simulation results in Fig. 2, the actual aperture of the liquid crystal lens is determined to be a circular area with a diameter of 1.56 mm centered at the origin of the liquid crystal lens in Fig. 3. By analyzing the effective area of the liquid crystal lens in Fig. 3, the focal length at different positions of the lens center is determined to be $8.2D$, and the aberration is $(0.1\pm0.02)\lambda$. The wavefront map of the lens is shown in Fig. 5, from which it can be seen that the wavefront of the lens remains unchanged.

Results and Discussions The dynamic foveated imaging system consists of a polarizer, an imaging telecentric lens group, a liquid crystal lens with a rectangular aperture, and a complementary metal-oxide-semiconductor (CMOS) device. Fig. 6 shows the experimental setup, while Fig. 7 shows the actual experimental setup. As can be seen from Fig. 6, a parallel beam of light is incident on the polarizer, with the polarization direction of the polarizer parallel to the rubbing direction of the liquid crystal lens. The polarized beam passes through the imaging telecentric lens and reaches the liquid crystal lens with a rectangular aperture. As shown in Fig. 3, the actual aperture diameter of the liquid crystal lens with a rectangular aperture is smaller than the clear aperture diameter, so part of the light reaching the CMOS is modulated, and thus a portion of the light is focused to form an image. In other words, the square aperture liquid crystal lens is located between the imaging telecentric lens group and the CMOS for focusing and real-time monitoring of the region of interest, with the focusing and real-time monitoring processes driven by an electric field, without any mechanical device. We select the driving conditions in Table 1 to drive the liquid crystal lens, with the center coordinates shown in Fig. 3. The circular area in Fig. 8 represents the actual position of the liquid crystal lens at different times, and the experimental results are shown in Fig. 9, indicating that the optical system has achieved dynamic foveated imaging. The modulation transfer function (MTF) test card ISO12233 is used to test the low resolution of the region of interest and the remaining areas (Fig. 10). It can be seen from Fig. 10 that the resolution of the foveated area is higher than that of the remaining areas.

Conclusions We aim to achieve dynamic foveated imaging by introducing a liquid crystal lens to alter the optical path difference. The electric field distribution of the moving center in the liquid crystal lens with a rectangular aperture is simulated and analyzed, and the corresponding interference fringes of the liquid crystal lens under the electric field distribution are measured by using a Mach-Zehnder interferometer. Experimental results show that the dynamic foveated imaging system can achieve high-resolution imaging of the region of interest while maintaining low-resolution imaging in other areas. Compared with traditional optical systems, the dynamic foveated imaging system has the advantages of compact structure, simple optical materials, high zero-order diffraction efficiency, and small transmission bandwidth. It can also scan different fields of view and perform high-resolution imaging, which makes it suitable for applications in scanning recognition, tracking, positioning, and other fields.

Key words imaging systems; dynamic foveated imaging; liquid crystal lens with rectangular aperture; high-resolution imaging